Measurement Report: Elevated excess-NH$_3$ can promote the redox reaction to produce HONO: Insights from the COVID-19 pandemic

Xinyuan Zhang[1,2], Lingling Wang[3], Nan Wang[3], Shuangliang Ma[3], Shenbo Wang[2,4] *, Ruiqin Zhang[2,4**], Dong Zhang[1,2], Mingkai Wang[2,4], Hongyu Zhang[1,2].

[1] College of Chemistry, Zhengzhou University, Zhengzhou, 450000, China

[2] Research Institute of Environmental Sciences, Zhengzhou University, Zhengzhou 450000, China

[3] Henan Provincial Ecological Environment Monitoring and Safety Center, Zhengzhou, 450000, China

[4] School of Ecology and Environment, Zhengzhou University, Zhengzhou, 450000, China

Correspondence: Shenbo Wang (shbwang@zzu.edu.cn) and Ruiqin Zhang (rqzhang@zzu.edu.cn)

Abstract

20 HONO plays a crucial role as a precursor to OH radicals in the tropospheric atmosphere.

21 The incongruity between HONO concentration and NO_x emissions during the COVID-

22 19 pandemic remains puzzling. Here, we show evidence from field observations of ten

23 sites in China that there was a noticeable increase in NH_3 concentrations during the

24 COVID-19 pandemic. In addition to the meteorological conditions, the significant

25 decrease in sulfate and nitrate concentrations enhanced the portioning of NH_4^+ to NH_3.

26 Such conditions enable enhanced particle pH values, which in turn accelerate the redox

27 reactions between NO_2 and SO_2 to form HONO. This mechanism partly explains the

28 lower reduction of HONO concentration than that of NO_2 concentration during the

29 pandemic and highlights the importance of coordinating the control of SO_2, NO_x, and

30 NH_3 emissions.

31 **Keywords:** Ammonia, HONO, Gas-particle portioning, Acidity, COVID-19 pandemic

1. Introduction

Nitrous acid (HONO) is a critical precursor of hydroxyl radical (OH), contributing to more than 60% of OH production (Alicke, 2003; Platt et al., 1980; Kleffmann et al., 2005). The OH can react with carbon monoxide, nitrogen oxides (NO_x), sulfur dioxide (SO_2), and volatile organic compounds to produce secondary pollutants such as ozone (O_3) and $PM_{2.5}$ (particulate matter with an aerodynamic diameter less than or equal to 2.5 μm), thereby affecting air quality, human health, and global climate change (Li et al., 2021a; Wang et al., 2023b; Lu et al., 2018)

High concentrations of HONO are present in urban daytime atmospheres, and exploring its sources has become a hot and challenging topic in the field of atmospheric chemistry (Jiang et al., 2022; Xu et al., 2019). Various sources of atmospheric HONO have been identified, including combustion processes (e.g., vehicle emissions) (Kramer et al., 2020; Liao et al., 2021; Li et al., 2021b), direct emissions from soil (Su and Zhang, 2011; Oswald et al., 2013; Meusel et al., 2018), homogeneous reactions between NO and OH radicals (Pagsberg et al., 1997; Atkinson et al., 2004), heterogeneous reactions of NO_2 on aerosols and ground surfaces (Zhang et al., 2020a; McFall et al., 2018; Liu et al., 2014, 2020a), and photolysis of nitrate (Spataro and Ianniello, 2014; Scharko et al., 2014; Romer et al., 2018; Ye et al., 2017; Shi et al., 2021). During the pandemic control periods, there was a substantial reduction in vehicle traffic flow and industrial emissions, leading to a decrease of more than 60% in NO_x emissions in eastern China (Huang et al., 2021a). It was initially expected that the concentration of HONO would also decrease proportionally. However, Liu et al. (2020b) observed that the decrease in

55 HONO concentration during the pandemic period was only 31%, which was

56 significantly lower than the reductions in NO (62%) and NO_2 (36%). Furthermore, the

57 observed concentrations of HONO during the COVID-19 pandemic in 2020 were

58 higher than those during the corresponding period in 2021 in Beijing (Luo et al., 2023).

59 These findings suggest the existence of a considerable unknown source of HONO

60 during the COVID-19 pandemic period.

61 Ammonia (NH_3) is a primary alkaline gas in the atmosphere, capable of influencing

62 the pH level of particulate matter and plays a crucial role in the atmospheric nitrogen

63 cycle (Gu et al., 2022; Xu et al., 2020; Gong et al., 2011). Several studies have indicated

64 that NH_3 can promote the formation of HONO by promoting the hydrolysis of NO_2 (Xu

65 et al., 2019) or the redox reaction of NO_2 with SO_2 (Liu et al., 2023). Moreover,

66 previous studies have reported that NH_3 concentrations in the atmosphere, particularly

67 in rural areas, significantly increased during the pandemic (Xu et al., 2022; Cui, 2023;

68 Zhang et al., 2020b). Consequently, the rise in NH_3 may contribute to the enhanced

69 formation of HONO (Huang et al., 2021a). Unfortunately, there is currently a lack of

70 research on the relationship between enhanced NH_3 and HONO during the COVID-19

71 pandemic period.

72 To address this, online observational data on the chemical composition of $PM_{2.5}$,

73 gaseous pollutants, and meteorological conditions at ten sites in China before and

74 during the COVID-19 pandemic period were analyzed to investigate the variation in

75 NH_3 concentrations and particle pH, and explore the promoting effect of increased pH

76 values on HONO formation.

2. Materials and methods

2.1 Observation sites

Online measurements were conducted at four urban and six rural sites in Henan Province, China from January 1 to February 29, 2020, including Sanmenxia (U-SMX), Zhoukou (U-ZK), Zhumadian (U-ZMD), and Xinyang (U-XY), as well as rural locations including Anyang (R-AY), Xinxiang (R-XX), Jiaozuo (R-JZ), Shangqiu (R-SQ), Nanyang (R-NY), and Puyang (R-PY). Descriptions and the spatial distribution of these ten sites can be found in Table S1 and Fig. S1.

2.2 Measurements

The aerosol and gas monitor (MARGA, Metrohm, Switzerland) was used to analyze the hourly water-soluble ions (Na^+, NH_4^+, K^+, Mg^{2+}, Ca^{2+}, Cl^-, NO_3^-, and SO_4^{2-}) in $PM_{2.5}$, as well as gaseous species (NH_3, HNO_3, HCl, and $HONO$) at ten sampling sites. The MARGA instrument is widely used (Chen et al., 2017; Stieger et al., 2019; Twigg et al., 2022). A detailed description of the instrument and QA/QC can be found in Text S1. In brief, the atmospheric sample passes through a $PM_{2.5}$ cut-off head, and both particles and gases enter a wet rotating dissolution device for diffusion. Subsequently, the particles in the sample undergo hygroscopic growth and condensation in an aerosol supersaturated vapor generator, followed by collection and ion chromatographic analysis. The gases in the sample are oxidized by H_2O_2 in the dissolution device, absorbed into a liquid solvent, and then entered the gas sample collection chamber for

97   ion chromatographic quantification. The range of minimum detection limits for water-

98   soluble ions was between 0.002 μg/m^3 (Cl$^-$) to 0.081 μg/m^3 (NH$_4^+$). Uncertainties of 20%

99   are assumed for the detection of NH$_3$ and NH$_4^+$, while uncertainties of 10% are assumed

100   for other components (Wang et al., 2020, 2022a). In addition, a detailed description of

101   HONO measurement using this system can be found in Text S2. Overall, the limit of

102   detection for HONO was 4 pptv and the uncertainty was estimated to be ± 20%.

103   The data for NO$_2$ and SO$_2$ were obtained from a series of instruments provided by

104   Thermo Fisher Scientific (USA). The hourly concentrations of organic carbon (OC) in

105   PM$_{2.5}$ were analyzed using a carbon analyzer (Model 4, Sunset Laboratory., USA).

106   Detailed descriptions of the NO$_2$, SO$_2$, and carbon analyzers can be found in Text S3.

107   The smart weather stations (LUFFTWS500, Sutron, Germany) were utilized for

108   synchronized observation of meteorological parameters including pressure,

109   temperature (T), and relative humidity (RH).

110   **2.3 Data analysis.**

111   **2.3.1 pH prediction.**

112   The thermodynamic model ISORROPIA-II was used to estimate the pH value of the

113   particles (Fountoukis, 2007) by inputting RH, T, K$^+$, Ca^{2+}, Mg^{2+}, total ammonia

114   ($TNH_x = 17 \times (\dfrac{[NH_4^+]}{18} + \dfrac{[NH_3]}{17})$), total sulfuric acid (TH$_2$SO$_4$, SO$_4^{2-}$), total sodium

115   (TNa, Na$^+$), total chlorine (TCl, Cl$^-$), and total nitrate (TNO$_3$ = NO$_3^-$ + HNO$_3$). The

116   model has two calculation modes: the forward mode and reverse mode, and the aerosol

117   dissolution systems can be set to simulate a metastable state (aqueous phase) or stable

118   state (aqueous and solid phase). Studies have shown that the forward mode is less

119   affected by instrument measurement errors than the reverse mode (Ding et al., 2019;

120   Song et al., 2018). Additionally, the minimum average RH of about 55% was recorded

121   during the sampling period at the ten sites. Thus, ISORROPIA-II was run in the forward

122   model for the aerosol system in the metastable condition and only used data with RH $\geq$

123   30% for simulation accuracy (Ding et al., 2019; Song et al., 2018). The ISORROPIA

124   model calculated the particle hydrate ion concentration per volume of air (H_{air}^+) and

125   aerosol water associated with inorganic matter (AWC_{inorg}). The pH value was calculated

126   using the following equation (Bougiatioti et al., 2016):

$$\text{pH} = -\log_{10} H_{aq}^+ = -\log_{10} \frac{1000 H_{air}^+}{AWC_{inorg} + AWC_{org}} \tag{2.1}$$

128   where the modeled concentrations for AWC_{inorg} and H_{air}^+ are $\mu g/m^3$, and AWC_{org} is the

129   particle water associated with the organic matters predicted using the following method:

$$AWC_{org} = \frac{m_s}{\rho_s} \frac{k_{org}}{\left(\frac{1}{RH} - 1\right)} \tag{2.2}$$

131   where m_s is the mass concentration of organic matter (OM = OC $\times$ f). The f is the

132   conversion factor of OC, which is dependent on the extent of OM oxidation and

133   secondary organic aerosol formation (Chow et al., 2015). Studies on the ratio of

134   OM/OC in fourteen cities in China suggested that the mean value of f was 1.59 $\pm$ 0.18

135   during the winter season in Northern China (Xing et al., 2013), and thus we adopted 1.6

136   as the f in this study. k_{org} is the organic hygroscopicity parameter and depends on organic

137   functionality, water solubility, molecular weight, and oxidation level. Han et al. (2022)

138   have reported that the k_{org} generally increased with O: C ratios, with a range of 0–0.3

139   for 23 organics, including carboxylic acids, amino acids, sugars, and alcohols. Gunthe

140   et al, (2011) estimated a $k_{org} = 0.06 \pm 0.01$ for the effective average hygroscopicity of

141   the non-refractory organic particulate matter in the aerosols in Beijing. Our previous

142   study has estimated that the uncertainties of k_{org} value (0.06) for pH in the range of 0–

143   0.3 only lead to –1–3% errors, which can be neglected (Wang et al., 2023a). Therefore,

144   the value of 0.06 was selected in this paper. ρ_s is the organic density, which was chosen

145   to be 1.35 g/cm^3 following previous studies (Table S2).

2.3.2 The sources of HONO

147   The sources of HONO include direct emission (P_{emi}), the homogeneous reaction of

148   NO and •OH (P_{OH+NO}), the heterogeneous reaction of NO_2 on the ground (P_{ground}) and

149   aerosol ($P_{aerosol}$), the photo-enhanced heterogeneous reaction of NO_2 on the ground

150   ($P_{ground+hv}$) and aerosol ($P_{aerosol+hv}$), and nitrate photolysis ($P_{nitrate}$). The detailed

151   calculation method is described in the Supplementary Material (Text S4, Table S3, Figs.

152   S2 and S3)

2.3.3 Redox reaction of NO_2 with SO_2.

154   The redox reaction of NO_2 with SO_2 (R_1) is considered a crucial potential source of

155   high concentrations of HONO in Northern China (Cheng et al., 2019; Wang et al.,

156   2016b):

157    $$S(IV) + 2NO_2 + H_2O \rightarrow S(VI) + 2H^+ + 2NO_2^- \tag{R_1}$$

158   the rate expression for reaction (R_1) was estimated to:

159            $d[S(VI)] / dt = k_1[NO_2][S(VI)],$ (2.3)

160   the rate constant k_1 value is pH dependent, e.g., for pH, 5, $k_1 = (1.4 \times 10^5 + 1.24 \times 10^7)/2$

161     $M^{-1} s^{-1}$. For k_1 values under other pH conditions and other related information, please

162   refer to Text S5, Table S4, and Table S5.

3. Results and discussion

3.1 Variations of NH_3, NH_4^+ and TNH_x.

165   The temporal variations of NH_3, NH_4^+, and TNH_x at 10 sampling sites in the pre-

166   COVID-19 pandemic period (PC, January 1 to 23, 2020) and during the COVID-19

167   pandemic period (DC, January 24 to February 29, 2020) are presented in Fig. 1, with

168   their average concentration listed in Table 1. In general, rural sites exhibited higher

169   concentrations of NH_3, NH_4^+, and TNH_x compared to urban sites, except for the R-NY

170   site. This finding is consistent with previous studies conducted in Zhengzhou (Wang et

171   al., 2020), Shanghai (Chang et al., 2019), and Quzhou (Feng et al., 2022a), owing to

172   the intense agricultural ammonia emissions. The highest concentrations of NH_3 and

173   TNH_x were recorded at site R-JZ, with average values of 25.3 ± 11.5 and 40.8 ± 20.1

174     $\mu g/m^3$, respectively. Site R-AY had the highest NH_4^+ concentration, measuring $19.3 \pm$

175     $12.9 \ \mu g/m^3$. Note that the current study area exhibited higher NH_3 levels compared to

176   other regions (Table S6), which probably was attributed to the highest NH_3 emissions

177   of Henan Province in China, primarily from nitrogen fertilizer application and livestock

178   farming (Wang et al., 2018; Ma, 2020).

179   Compared to the PC, NH_3 concentrations increased in the DC at all sites. Notably,

180   rural sites experienced more significant increases in NH_3 concentrations than urban

181   sites, which was similar to the trend in Shanghai (Xu et al., 2022). The largest increases

182   in NH_3 concentrations were observed at R-SQ (71%, 7.3 μg/m^3) and U-ZK (37%, 4.8

183   μg/m^3) for rural and urban sites, respectively. In contrast, the concentrations of NH_4^+

184   and TNH_x decreased in the DC with the largest reduction at rural site R-PY (51%, 12.9

185   μg/m^3) and urban site U-ZMD (48%, 9.3 μg/m^3). Regarding TNH_x, rural sites exhibited

186   larger reductions, with site R-SQ experiencing the largest decrease of 37% (4.7 μg/m^3).

187   Figure 2 illustrates the spatial distribution and the diurnal variation of NH_3

188   concentrations at the ten sites before and during the pandemic. NH_3 concentrations in

189   most sites exhibited an unimodal trend in PC that NH_3 concentrations gradually

190   increased after sunrise, reaching a peak around noon (11:00–12:00), and then decreased

191   to a valley around 16:00–17:00. This diurnal pattern is similar to NH_3 variations

192   observed in urban areas of Houston, USA, as a result of the natural emissions from

193   vegetation and soil during photosynthesis (Gong et al., 2011). However, other studies

194   have recorded a significant NH_3 peak during the early morning of 8:00–10:00 (Ellis et

195   al., 2011; Meng et al., 2018; Gu et al., 2022), suggesting the influence of vehicle

196   emissions (Gong et al., 2011; Gu et al., 2022), residual NH_3 mixing, soil or plant

197   emissions (Ellis et al., 2011), and dew volatilization (Wentworth et al., 2016; Huang et

198   al., 2021b). Therefore, the NH_3 in urban and rural areas of this study was probably less

199   affected by NH_3 emissions from vehicles, different from the recent studies in megacities

200   of China (e.g., Beijing and Shanghai) (Gu et al., 2022; Wu et al., 2023; Zhang et al.,

201 2020b). In addition to the transport from agricultural emissions, urban NH_3 in this

202 region might also originate from other non-agricultural sources, such as wastewater

203 treatment, coal combustion, household waste, urban green spaces, and human

204 excrement (Chang et al., 2019).

205   During the COVID-19 pandemic, the diurnal variation of NH_3 in both urban and rural

206 sites still maintained an unimodal distribution. The peak values in urban sites remained

207 consistent with PC levels, further demonstrating that the influence of vehicles on NH_3

208 in urban areas was limited. Notably, the peak time of NH_3 in rural sites shifted 1–2 hours

209 earlier compared to the trend in PC. Ammonia in rural areas primarily originates from

210 nitrogen fertilizer application, livestock, and poultry breeding (Feng et al., 2022b;

211 Meng et al., 2018), which are significantly influenced by T and RH (Liu et al., 2023).

212 Table S7 and Fig. S4 reveal that there was an increased T and a decreased RH at rural

213 sites in the DC than the PC, which could accelerate the evaporation of NH_3 and thus

214 potentially lead to earlier peak NH_3 concentrations.

215 **3.2 Gas-to-particle conversion of NH_3**

216   The increased NH_3 accompanying decreased NH_4^+ in the DC suggests that the gas-

217 particle partition of NH_3/ NH_4^+ may determine the elevated NH_3 concentrations.

218 Meteorological parameters, including RH and T, play a crucial role in the gas-particle

219 partitioning of NH_3 (Liu et al., 2023; Xu et al., 2020). Therefore, the higher T and lower

220 RH in the DC (Table S7 and Fig. S4) favored the conversion of NH_4^+ to NH_3, resulting

221 in a decrease in $\varepsilon(NH_4^+)$ ($[NH_4^+]/([NH_3] + [NH_4^+])$) compared to those in the PC (Table

222   S7).

223   NH$_3$ primarily enters particles to neutralize acidic ions (Wang et al., 2020; Xu et al.,

224   2020; Liu et al., 2017; Ye et al., 2011; Wells, 1998). Accordingly, the concentrations of

225   required ammonia (Required-NH$_x$) and excess ammonia (Excess-NH$_x$) were calculated

226   based on the acidic substances as follows (Wang et al., 2020):

227
$$\text{Required-NH}_x = 17 \times \left(\frac{[\text{SO}_4^{2-}]}{48} + \frac{[\text{NO}_3^-]}{63} + \frac{[\text{Cl}^-]}{35.5} + \frac{[\text{HNO}_3]}{64} + \frac{[\text{HCl}]}{36.5}\right) \\ - 17 \times \left(\frac{[\text{Na}^+]}{23} + \frac{[\text{K}^+]}{39} + \frac{[\text{Ca}^{2+}]}{20} + \frac{[\text{Mg}^{2+}]}{12}\right) \tag{3.1}$$

228
$$\text{Excess-NH}_x = \text{TNH}_x - \text{Required-NH}_x \tag{3.2}$$

229   where [W] represents the concentration of the substance (μg/m^3). The significant linear

230   fitting (R^2 is greater than 0.96, and the slope is close to 1) in Fig. S5 demonstrates that

231   the anions and cations at each site were close to the equilibrium state. Therefore, the

232   organic acids in PM$_{2.5}$ may have less effect on NH$_3$ and NH$_4^+$ and were not considered

233   in Formula 3.1.

234   As shown in Fig. 3 and Table S8, compared to those in the PC, the concentration of

235   Required-NH$_x$ in the DC significantly decreased (ranging from 37% at site R-JZ to 58%

236   at site R-PY), while the concentration of Excess-NH$_x$ increased (ranging from 9% at

237   site R-AY to 78% at site R-SQ). The reduction in the concentrations of sulfate and

238   nitrate (Fig. S6) was responsible for the decrease in the concentration of Required-NH$_x$.

239   To sum up, in addition to meteorological conditions, the substantial reduction in

240   anthropogenic emissions of SO$_2$, NO$_x$, and other pollutants in the DC had led to a

241   decrease in acidic substances (e.g., sulfate and nitrate) in particles, in turn, resulting in

242   more gas-phase NH$_3$ concentration remaining in the atmosphere.

3.3 Particle pH before and during COVID-19

Diurnal patterns of particle pH in PC and DC at ten sites are summarized in Fig. 4 with their average values listed in Table S9. $PM_{2.5}$ shows consistent moderate acidity, with mean values in the range of 4.2–5.1, which were close to the values in previous studies (Table S9). Compared to the PC, the particle pH at ten sites increased obviously in the DC, with the highest increase of 0.5 (U-ZK) and 0.3 (R-PY) at urban and rural sites, respectively, which were the subject of in-depth discussion in the following text.

To explore the dominant factors that determine the local particle pH level and result in the high pH during the DC, sensitivity tests of pH to chemical species (i.e., TNH_x, TH_2SO_4, TNO_3, TCl, TNa, K^+, Ca^{2+}, and Mg^{2+}) and meteorological parameters (i.e., T and RH) were performed. A given range for a variable (i.e., TNH_x) with corresponding average values of other parameters (i.e., TH_2SO_4, TNO_3, TCl, TNa, K^+, Ca^{2+}, Mg^{2+}, T, and RH) was input into the model and simulated to compare its effects on pH. As shown in Fig. S7, pH increases with the cation concentrations (i.e., TNH_x, Na^+, K^+, Ca^{2+}, and Mg^{2+}) increasing as well as the anion concentrations (i.e., TH_2SO_4, TNO_3, and Cl^-), T and RH decreasing. According to the average values of input data during PC (Blue line in Fig. S7) and DC (Red line in Fig. S7) at U-ZK and R-PY sites respectively, the changes in pH (ΔpH in Fig. 5) indicate that the decrease in TNH_x concentration and the increase in T in DC led to a decrease in pH values (ΔpH: 0.09 at U-ZK and 0.08 at R-PY sites) compared to PC. However, this effect was outweighed by the decrease in TH_2SO_4 (ΔpH: 0.07 and 0.8 at U-ZK and R-PY sites, respectively) and TNO_3 (ΔpH: 0.05 and 0.4 at U-ZK and R-PY sites, respectively) concentrations as well as the

265 increase in K^+ (ΔpH: 0.03 at U-ZK and 0.2 at R-PY site) and Mg^{2+} (ΔpH: 0.01 at U-ZK

266 and 0.04 at R-PY site) concentrations in the DC, and resulting in an overall increase in

267 pH values in the DC. Furthermore, the relationship between particle pH with the

268 concentrations of Required-NH_x, and Excess-NH_x, which considers all chemical

269 components, is investigated to examine the dominant factor on the increasing pH in DC.

270 As shown in Fig. 6, the higher Excess-NH_x concentrations in the DC led to higher

271 increases in pH values (ΔpH: 1 at U-ZK and 0.5 at R-PY site) than those in PC (ΔpH:

272 0.3 at U-ZK and 0.2 at R-PY site), thus Excess-NHx concentrations may be the key

273 factor in promoting the pH values.

274 3.4 The influence of pH on HONO.

275 The observed HONO concentrations decreased by 18% and 54% at U-ZK (0.8 ppb)

276 and R-PY (0.9 ppb) sites in the DC, respectively, compared to those (1.0 and 2.2 ppb)

277 in the PC. Moreover, all the known HONO production sources rates including P_{emi}, P_{OH}

278 $_{+ NO}$, P_{ground}, $P_{ground+hv}$, $P_{aerosol}$, $P_{aerosol+hv}$, and $P_{nitrate}$ (Fig. 7) show a decreasing trend from

279 PC to DC, with the total reductions of 42% and 80% for U-ZK and R-PY, respectively.

280 At the U-ZK, $P_{ground+hv}$ decreased the most (84%), while at the R-PY, $P_{nitrate}$ had the

281 largest decrease about 85%, which was speculated to be related to the decrease of NO_x

282 and NO_3^- concentration in DC. Note that the reduction rates in the overall known source

283 and almost individual sources were greater than the reduction rates in HONO

284 concentrations (Figs. 7 and 8), thus we hypothesized that there should be other sources

285 capable of promoting HONO production. Soil emission has been demonstrated to be a

286 major source of HONO, which is affected by temperature to some extent (Liu et al.,

287 2020b, 2020c). However, there was no significant positive correlation with temperature

288 in Fig. S8, and temperatures did not exceed 10°C during the study periods, suggesting

289 that soil emission may not be a major contributor to HONO. Note that there were

290 positive correlations between HONO with SO_2, Excess-NH_x, SO_4^{2-}, and pH (Fig. S8)

291 indicating that the R_1 reaction might form an amount of HONO and contribute to less

292 reduction in the observed HONO concentrations.

293 Considering that R_1 mainly reacts in the liquid phase, the calculated reaction rates of

294 R_1 under the conditions of RH > 60% in the PC and DC periods are illustrated in Figs.

295 8 and S9. Despite the decrease in NO_2 and SO_2 concentrations in the DC, the increase

296 in particle pH, increasing HSO_3^- concentration in the aqueous phase, promoted the R_1

297 reaction rates by 58% and 59% at U-ZK and R-PY (Figure 8), respectively.

298 Consequently, the enhanced R_1 reaction might prevent a large decrease in HONO (18%

299 at U-ZK and 53% at R-PY) under the conditions of a significant reduction in vehicle

300 emissions and a decline of 66% and 69% in NO_2 concentrations at U-ZK and R-PY,

301 respectively.

302 **3.5 Uncertainty**

303 According to sensitivity tests of pH (Fig. S7) and R_1 (Fig. S10), pH increases with

304 the concentrations of cations (TNH_x, TNa, K^+, Ca^{2+}, and Mg^{2+}) and OC increasing as

305 well as anions (TH_2SO_4, TNO_3, and Cl^-) concentrations, T, and RH decreasing. R_1

306 reaction rate increases with the concentrations of AWC, NO_2, SO_2, pH, and pressure,

307   while increasing as well as T decreasing. Therefore, two extreme scenarios (i.e., the

308   maximum and minimum rate scenarios) were evaluated to estimate the uncertainty of

309   pH, and R_1 based on the measurement uncertainties at the U-ZK and R-PY sites. Figure

310   S11 suggests that the two extreme scenarios can be led to –10–7% and –71–125%

311   uncertainties at the U-ZK site and –10–7% and –78–123% uncertainties at the R-PY

312   site for pH and R_1, respectively.

313   4. Conclusions

314   Elevated NH_3 concentration was observed during the COVID-19 pandemic at both

315   urban and rural sites in China. In addition to the rise in T and decrease in RH during the

316   COVID-19 pandemic, which favored the conversion of NH_4^+ to NH_3, the significant

317   decrease in sulfate and nitrate concentrations led to the decline in Required-NH_x and

318   was beneficial to the particle-phase NH_4^+ portioning to gas-phase NH_3. Furthermore,

319   under the environmental conditions of increased NH_3 concentration and decreased

320   acidic substance concentration, the pH values increased by 0.5 and 0.3 at U-ZK and R-

321   PY increased during the pandemic, respectively. Consequently, the high pH values

322   accelerated the formation rate of HONO through the oxidation-reduction reaction of

323   NO_2 with SO_2 (an increase of 58% at U-ZK and 59% at R-PY, respectively), partially

324   compensating for the decrease in HONO concentration caused by the decline in vehicle

325   emissions, NO_2 and NO_3^- concentrations during the COVID-19 pandemic.

5. Implications

HONO plays a crucial role as a precursor to OH radicals in the tropospheric atmosphere (Xue, 2022). There have been significant observations of high HONO concentrations in urban areas during the daytime, leading to a growing interest in understanding its sources in atmospheric chemistry (Jiang et al., 2022; Xu et al., 2019). The heterogeneous reaction mechanism of NO_2 on aerosol surfaces is currently the focus of research on HONO sources, particularly in regions with elevated levels of atmospheric particulate matter, where it could potentially become a major contributor to HONO production (Zhang et al., 2022; Liao et al., 2021). One of the pathways for heterogeneous reactions on aerosol surfaces is the redox reaction of NO_2 with SO_2. However, the significance of this reaction in HONO production in the real atmosphere is often overlooked, as it relies on the high pH of aerosols (Ge et al., 2019). In recent years, there has been increasing attention on the enhancing effect of NH_3 on the redox reaction, with laboratory experiments demonstrating its ability to generate substantial amounts of HONO (Ge et al., 2019). This study highlights the importance of this reaction based on actual atmospheric observations. Furthermore, numerous studies have indicated that if control over NH_3 emissions continues to relax while SO_2 and NO_2 emissions decrease, the particle pH in future China is expected to rise steadily (Xie et al., 2020; Song et al., 2019; Wang et al., 2020). Consequently, the redox reaction of NO_2 with SO_2 could become a significant source of HONO in China. Therefore, it is crucial to coordinate the control of SO_2, NO_x, and NH_3 emissions to avoid a rapid increase in the particle pH.

348

Data availability: All the data presented in this article can be accessed through

https://zenodo.org/records/10273539. (Zhang, 2023).

351

Author contributions. XZ Data Curation, Writing - Original Draft, Visualization. LW, NW, SM, and DZ Investigation, Visualization, Data Curation. DZ, HZ, and MW Investigation. SW Conceptualization, Data Curation, Supervision. RZ Data Curation, Funding acquisition. All people are involved in the discussion of the results.

356

Competing interest. The authors declare no competing financial interest.
358
Acknowledgments. This work was supported by the China Postdoctoral Science Foundation (2023M733220), the Zhengzhou $PM_{2.5}$ and O_3 Collaborative Control and Monitoring Project (20220347A), and the National Key Research and Development Program of China (No. 2017YFC0212403).

References

Alicke, B.: OH formation by HONO photolysis during the BERLIOZ experiment, J. Geophy. Res.; 108, 8247, https://doi.org/10.1029/2001JD000579, 2003.

Atkinson, R., Baulch, D.L., Cox, R.A., Crowley, J.N., Hampson, R.F., Hynes, R.G., Jenkin, M.E., and Rossi, M. J., Troe, J.: Evaluated kinetic and photochemical data for atmospheric chemistry: volume I - gas phase reactions of O_x, HO_x, NO_x and SO_x species., Atmos. Chem. Phys., 4,1461–1738, https://doi.org/10.5194/acp-4-1461-2004, 2004.

Bougiatioti, A., Nikolaou, P., Stavroulas, I., Kouvarakis, G., Weber, R., Nenes, A., Kanakidou, M., and Mihalopoulos, N.: Particle water and pH in the eastern Mediterranean: source variability and implications for nutrient availability, Atmos. Chem. Phys., 16, 4579–4591, https://doi.org/10.5194/acp-16-4579-2016, 2016.

Chang, Y., Zou, Z., Zhang, Y., Deng, C., Hu, J., Shi, Z., Dore, A. J., and Collett, J. L., Jr.: Assessing contributions of agricultural and nonagricultural emissions to atmospheric ammonia in a Chinese megacity. Environ. Sci. Technol. 53, 1822–1833., https://doi.org/10.1021/acs.est.8b05984, 2019.

Chen, X., Walker, J. T., and Geron, C.: Chromatography related performance of the monitor for aerosols and gases in ambient air (MARGA): laboratory and field-based evaluation. Atmos. Meas. Tech. 10, 3893–3908. https://doi.org/10.5194/amt-10-3893-2017, 2017.

Cheng, Y., Zheng, G., Wei, C., Mu, Q., Zheng, B., Wang, Z., Gao, M., Z., Q., He, K., Carmichael, G., Pöschl, U., and Su, and H.: Reactive nitrogen chemistry in aerosol

385   water as a source of sulfate during haze events in China, Sci. Adv. 2, e1601530.,

386   https://doi.org/10.1126/sciadv.1601530, 2019.

387   Chow, J. C., Lowenthal, D. H., Chen, L. W. A., Wang, X., and Watson, J. G.: Mass

388   reconstruction methods for $PM_{2.5}$: a review, Air Qual. Atmos. Health., 8, 243 – 263,

389   https://doi.org/10.1007/s11869-015-0338-3, 2015.

390   Cui, L.: Impact of COVID-19 restrictions on the concentration and source

391   apportionment of atmospheric ammonia (NH_3) across India, Sci. Total Environ.,

392   881, https://doi.org/10.1016/j.scitotenv.2023.163443, 2023.

393   Ding, J., Zhao, P., Su, J., Dong, Q., Du, X., and Zhang, Y.: Aerosol pH and its driving

394   factors in Beijing, Atmos. Chem. Phys. 19, 7939–7954.,

395   https://doi.org/10.5194/acp-19-7939-2019, 2019.

396   Ellis, R. A., Murphy, J. G., Markovic, M. Z., VandenBoer, T. C., Makar, P. A., Brook,

397   J., and Mihele, C.: The influence of gas-particle partitioning and surface-

398   atmosphere exchange on ammonia during BAQS-Met, Atmos. Chem. Phys. 11,

399   133–145., https://doi.org/10.5194/acp-11-133-2011, 2011.

400   Feng, S., Xu, W., Cheng, M., Ma, Y., Wu, L., Kang, J., Wang, K., Tang, A., Collett, J.

401   L., Fang, Y., Goulding, K., Liu, X., and Zhang, F.: Overlooked nonagricultural and

402   wintertime agricultural NH_3 emissions in Quzhou county, north China plain:

403   evidence from ^{15}N-Stable Isotopes. Environ. Sci. Technol. Lett. 9, 127–133,

404   https://doi.org/10.1021/acs.estlett.1c00935, 2022a.

405   Feng, T., Zhao, S., Liu, L., Long, X., Gao, C., and Wu, N.: Nitrous acid emission from

406   soil bacteria and related environmental effect over the North China Plain, Chemos.,

407   287, https://doi.org/10.1016/j.chemosphere.2021.132034, 2022b.

408   Fountoukis, C., Nenes, A.: ISORROPIA II: a computationally efficient thermodynamic

409   equilibrium model for K^+-Ca^{2+}-Mg^{2+}-NH_4^+-Na^+-SO_4^{2-}-NO^{3-}-Cl^--H_2O aerosols.

410   Atmos. Chem. Phys. 7, 4639–4659, https://doi.org/10.5194/acp-7-4639-2007,

411   2007.

412   Ge, S., Wang, G., Zhang, S., Li, D., and Zhang, H.: Abundant NH_3 in China enhances

413   atmospheric HONO production by promoting the heterogeneous reaction of SO_2

414   with NO_2. Environ. Sci. Technol. 53, 14339–14347,

415   https://doi.org/10.1021/acs.est.9b04196, 2019.

416   Gong, L., Lewicki, R., Griffin, R. J., Flynn, J. H., Lefer, B. L., and Tittel, F. K.:

417   Atmospheric ammonia measurements in Houston, TX using an external-cavity

418   quantum cascade laser-based sensor, Atmos. Chem. Phys. 11, 9721–9733,

419   https://doi.org/10.5194/acp-11-9721-2011, 2011.

420   Gu, M., Pan, Y., Walters, W. W., Sun, Q., Song, L., Wang, Y., Xue, Y., and Fang, Y.:

421   ehicular emissions enhanced ammonia concentrations in winter mornings: insights

422   from diurnal nitrogen isotopic signatures. Environ. Sci. Technol. 56, 1578–1585,

423   https://doi.org/10.1021/acs.est.1c05884, 2022.

424   Gunthe, S. S., Rose, D., Su, H., Garland, R. M., Achtert, P., Nowak, A., Wiedensohler,

425   A., Kuwata, M., Takegawa, N., Kondo, Y., Hu, M., Shao, M., Zhu, T., Andreae, M.

426   O., and Pöschl, U.: Cloud condensation nuclei (CCN) from fresh and aged air

427   pollution in the megacity region of Beijing, Atmos. Chem. Phys., 11, 11023 –

428   11039, https://doi.org/10.5194/acp-11-11023-2011, 2011.

429   Han, S., Hong, J., Luo, Q., Xu, H., Tan, H., Wang, Q., Tao, J., Zhou, Y., Peng, L., He,

430   Y., Shi, J., Ma, N., Cheng, Y., and Su, H.: Hygroscopicity of organic compounds

431   as a function of organic functionality, water solubility, molecular weight, and

432   oxidation level, Atmos. Chem. Phys., 22, 3985–4004, https://doi.org/10.5194/acp-

433   22-3985-2022, 2022.

434   Huang, X., Ding, A., Gao, J., Zheng, B., Zhou, D., Qi, X., Tang, R., Wang, J., Ren, C.,

435   Nie, W., Chi, X., Xu, Z., Chen, L., Li, Y., Che, F., Pang, N., Wang, H., Tong, D.,

436   Qin, W., Cheng, W., Liu, W., Fu, Q., Liu, B., Chai, F., Davis, S. J., Zhang, Q., and

437   He, K.: Enhanced secondary pollution offset reduction of primary emissions

438   during COVID-19 lockdown in China, Natl Sci Rev, 8, nwaa137,

439   https://doi.org/10.1093/nsr/nwaa137, 2021a.

440   Huang, X., Zhang, J., Zhang, W., Tang, G., and Wang, Y.: Atmospheric ammonia and

441   its effect on $PM_{2.5}$ pollution in urban Chengdu, Sichuan Basin, China. Environ.

442   Pollut. 291, 118–195. https://doi.org/10.1016/j.envpol.2021.118195, 2021b.

443   Jiang, Y., Xue, L., Shen, H., Dong, C., Xiao, Z., and Wang, W.: Dominant processes of

444   HONO derived from multiple field observations in contrasting environments.

445   Environ.   Sci.   Technol.   Lett.   9,   258–264,

446   https://doi.org/10.1021/acs.estlett.2c00004, 2022.

447   Kleffmann, J., Gavriloaiei, T., Hofzumahaus, A., Holland, F., Koppmann, R., Rupp, L.,

448   Schlosser, E., Siese, M., and Wahner, A.: Daytime formation of nitrous acid: A

449   major source of OH radicals in a forest, Geophys. Res. Lett., 32,

450   https://doi.org/10.1029/2005gl022524, 2005.

451   Kramer, L. J., Crilley, L. R., Adams, T. J., Ball, S. M., Pope, F. D., and Bloss, W. J.:

452   Nitrous acid (HONO) emissions under real-world driving conditions from vehicles

453   in   a   UK   road   tunnel,   Atmos.   Chem.   Phys.   20,   5231–5248,

454   https://doi.org/10.5194/acp-20-5231-2020, 2020.

455   Li, J., An, X., Cui, M., Sun, Z., Wang, C., and Li, Y.: Simulation study on regional

456   atmospheric oxidation capacity and precursor sensitivity, Atmos. Environ. 263,

457   118657, https://doi.org/10.1016/j.atmosenv.2021.118657, 2021a.

458   Li, S., Song, W., Zhan, H., Zhang, Y., Zhang, X., Li, W., Tong, S., Pei, C., Wang, Y.,

459   Chen, Y., Huang, Z., Zhang, R., Zhu, M., Fang, H., Wu, Z., Wang, J., Luo, S., Fu,

460   X., Xiao, S., Huang, X., Zeng, J., Zhang, H., Chen, D., Gligorovski, S., Ge, M.,

461   George, C., and Wang, X.: Contribution of vehicle emission and NO_2 surface

462   conversion to nitrous acid (HONO) in urban environments: implications from tests

463   in   a   tunnel.   Environ.   Sci.   Technol.,   55,   15616–15624,

464   https://doi.org/10.1021/acs.est.1c00405, 2021.

465   Liao, S., Zhang, J., Yu, F., Zhu, M., Liu, J., Ou, J., Dong, H., Sha, Q., Zhong, Z., Xie,

466   Y., Luo, H., Zhang, L., and Zheng, J.: High gaseous nitrous acid (HONO)

467   emissions from light-duty diesel vehicles. Environ. Sci. Technol. 55, 200–208,

468   https://doi.org/10.1021/acs.est.0c05599, 2021.

469   Liu, J., Deng, H., Lakey, P. S. J., Jiang, H., Mekic, M., Wang, X., Shiraiwa, M., and

470   Gligorovski, S.: Unexpectedly high indoor HONO concentrations associated with

471   photochemical NO_2 transformation on glass windows. Environ. Sci. Technol. 54,

472   15680–15688, https://doi.org/10.1021/acs.est.0c05624, 2020a.

473   Liu, M., Song, Y., Zhou, T., Xu, Z., Yan, C., Zheng, M., Wu, Z., Hu, M., Wu, Y., and

474   Zhu, T.: Fine particle pH during severe haze episodes in northern China. Geophys.

475   Res. Lett. 44, 5213–5221, https://doi.org/10.1002/2017gl073210, 2017.

476   Liu, P., Chen, H., Song, Y., Xue, C., Ye, C., Zhao, X., Zhang, C., Liu, J., and Mu, Y.:

477   Atmospheric ammonia in the rural North China Plain during wintertime: variations,

478   sources, and implications for HONO heterogeneous formation. Sci. Total. Environ.

479   861, 160768, https://doi.org/10.1016/j.scitotenv.2022.160768, 2023.

480   Liu, Y., Ni, S., Jiang, T., Xing, S., Zhang, Y., Bao, X., Feng, Z., Fan, X., Zhang, L., and

481   Feng, H.: Influence of Chinese New Year overlapping COVID-19 lockdown on

482   HONO   sources   in   Shijiazhuang,   Sci.   Total   Environ.,   745,   141025,

483   https://doi.org/10.1016/j.scitotenv.2020.141025, 2020b.

484   Liu, Y., Zhang, Y., Lian, C., Yan, C., Feng, Z., Zheng, F., Fan, X., Chen, Y., Wang, W.,

485   Chu, B., Wang, Y., Cai, J., Du, W., Daellenbach, K. R., Kangasluoma, J., Bianchi,

486   F., Kujansuu, J., Petäjä, T., Wang, X., Hu, B., Wang, Y., Ge, M., He, H., and

487   Kulmala, M.: The promotion effect of nitrous acid on aerosol formation in

488   wintertime in Beijing: The possible contribution of traffic-related emissions,

489   Atmos. Chem. Phys, 20, 13023–13040, https://doi.org/10.5194/acp-20-13023-

490   2020, 2020c.

491   Liu, Z., Wang, Y., Costabile, F., Amoroso, A., Zhao, C., Huey, L. G., Stickel, R., Liao,

492   J., and Zhu, T.: Evidence of aerosols as a media for rapid daytime HONO

493   production   over   China,   Environ.   Sci.   Technol.,   48,   13023–13040,

494   https://doi.org/10.1021/es504163z, 2014.

495   Lu, K., Guo, S., Tan, Z., Wang, H., Shang, D., Liu, Y., Li, X., Wu, Z., Hu, M., and

496   Zhang, Y.: Exploring atmospheric free-radical chemistry in China: the self-

497   cleansing capacity and the formation of secondary air pollution, Natl. Sci. Rev., 6,

498   579-594, https://doi.org/10.1093/nsr/nwy073, 2018.

499   Luo, L., Bai, X., Lv, Y., Liu, S., Guo, Z., Liu, W., Hao, Y., Sun, Y., Hao, J., Zhang, K.,

500   Zhao, H., Lin, S., Zhao, S., Xiao, Y., Yang, J., and Tian, H.: Exploring the driving

501   factors of haze events in Beijing during Chinese New Year holidays in 2020 and

502   2021 under the influence of COVID-19 pandemic, Sci. Total Environ., 859,

503   160172, https://doi.org/10.1016/j.scitotenv.2022.160172, 2023.

504   Ma, S.: High-resolution assessment of ammonia emissions in China: Inventories,

505   driving   forces   and   mitigation,   Atmos.   Environ.,   229,

506   https://doi.org/10.1016/j.atmosenv.2020.117458, 2020.

507   McFall, A. S., Edwards, K. C., and Anastasio, C.: Nitrate photochemistry at the air-ice

508   interface and in other ice reservoirs, Environ. Sci. Technol., 52, 5710–5717,

509   https://doi.org/10.1021/acs.est.8b00095, 2018.

510   Meng, Z., Xu, X., Lin, W., Ge, B., Xie, Y., Song, B., Jia, S., Zhang, R., Peng, W., Wang,

511   Y., Cheng, H., Yang, W., and Zhao, H.: Role of ambient ammonia in particulate

512   ammonium formation at a rural site in the North China Plain, Atmos. Chem. Phys.,

513   18, 167–184, https://doi.org/10.5194/acp-18-167-2018, 2018.

514   Meusel, H., Tamm, A., Kuhn, U., Wu, D., Leifke, A. L., Fiedler, S., Ruckteschler, N.,

515   Yordanova, P., Lang-Yona, N., Pöhlker, M., Lelieveld, J., Hoffmann, T., Pöschl,

516   U., Su, H., Weber, B., and Cheng, Y.: Emission of nitrous acid from soil and

517   biological soil crusts represents an important source of HONO in the remote

518   atmosphere   in   Cyprus,   Atmos.   Chem.   Phys.,   18,   799 – 813,

519   https://doi.org/10.5194/acp-18-799-2018, 2018.

520   Oswald, R., Behrendt, T., Ermel, M., Wu, D., Su, H., Cheng, Y., Breuninger, C.,

521   Moravek, A., Mougin, E., Delon, C., Loubet, B., Pommerening-Roser, A., Sorgel,

M., Poschl, U., and Hoffmann, T., Andreae, M.O., Meixner, F.X., Trebs, I.: HONO

emissions from soil bacteria as a major source of atmospheric reactive nitrogen.,

Science. 341, 1233–1235, https://www.science.org/doi/10.1126/science.1242266,

2013.

Pagsberg, P., Bjergbakke, E., Ratajczak, E., Sillesen, A.: Kinetics of the gas phase

reaction OH + NO (+M)$^-$ > HONO (+M) and the determination of the UV

absorption cross sections of HONO., Chem. Phys. Lett. 272, 383–390,

https://doi.org/10.1016/s0009-2614(97)00576-9, 1997.

Platt, U., Perner, D., Harris, G. W., Winer, A. M., and Pitts, J. N.: Observations of

nitrous acid in an urban atmosphere by differential optical absorption, Nature, 285,

312–314, https://doi.org/10.1038/285312a0, 1980.

Romer, P. S., Wooldridge, P. J., Crounse, J. D., Kim, M. J., Wennberg, P. O., Dibb, J.

E., Scheuer, E., Blake, D. R., Meinardi, S., Brosius, A. L., Thames, A. B., Miller,

D. O., Brune, W. H., Hall, S. R., Ryerson, T. B., and Cohen, R. C.: Constraints on

aerosol nitrate photolysis as a potential source of HONO and NO$_x$. Environ. Sci.

Technol. 52, 13738–13746, https://doi.org/10.1021/acs.est.8b03861, 2018.

Scharko, N. K., Berke, A. E., and Raff, J. D.: Release of nitrous acid and nitrogen

dioxide from nitrate photolysis in acidic aqueous solutions, Environ. Sci. Technol.,

48, 11991–12001, https://doi.org/10.1021/es503088x, 2014.

Shi, Q., Tao, Y., Krechmer, J. E., Heald, C. L., Murphy, J. G., Kroll, J. H., and Ye, Q.:

Laboratory investigation of renoxification from the photolysis of inorganic

particulate nitrate, Environ. Sci. Technol., 55, 854–861,

544   https://doi.org/10.1021/acs.est.0c06049, 2021.

545 Song, S., Gao, M., Xu, W., Shao, J., Shi, G., Wang, S., Wang, Y., Sun, Y., and McElroy,

546   M. B.: Fine-particle pH for Beijing winter haze as inferred from different

547   thermodynamic equilibrium models, Atmos. Chem. Phys., 18, 7423–7438,

548   https://doi.org/10.5194/acp-18-7423-2018, 2018.

549 Song, S., Nenes, A., Gao, M., Zhang, Y., Liu, P., Shao, J., Ye, D., Xu, W., Lei, L., Sun,

550   Y., Liu, B., Wang, S., and McElroy, M. B.: Thermodynamic modeling suggests

551   declines in water uptake and acidity of inorganic aerosols in Beijing winter haze

552   events during 2014/2015–2018/2019. Environ. Sci. Technol. Lett. 6, 752–760,

553   https://doi.org/10.1021/acs.estlett.9b00621, 2019.

554 Spataro, F., and Ianniello, A.: Sources of atmospheric nitrous acid: state of the science,

555   current research needs, and future prospects, J. Air. Waste. Manag. Assoc., 64,

556   1232–1250, https://doi.org/10.1080/10962247.2014.952846, 2014.

557 Stieger, B., Spindler, G., van Pinxteren, D., Grüner, A., Wallasch, M., and Herrmann,

558   H.: Development of an online-coupled MARGA upgrade for the 2 h interval

559   quantification of low-molecular-weight organic acids in the gas and particle phases,

560   Atmos. Meas. Tech. 12, 281–298, https://doi.org/10.5194/amt-12-281-2019, 2019.

561 Su, H., Cheng, Y., Oswald, R., Behrendt, T., Trebs, I., Meixner, F.X., Andreae, M.O.,

562   Cheng, P., and Zhang, Y., Poschl, U.: Soil nitrite as a source of atmospheric HONO

563   and   OH   radi   cals.,   Science.   333,   1616–1618,

564   https://doi.org/10.1126/science.1207687, 2011.

565 Twigg, M. M., Berkhout, A. J. C., Cowan, N., Crunaire, S., Dammers, E., Ebert, V.,

566   Gaudion, V., Haaima, M., Häni, C., John, L., Jones, M. R., Kamps, B., Kentisbeer,

567   J., Kupper, T., Leeson, S. R., Leuenberger, D., Lüttschwager, N. O. B., Makkonen,

568   U., Martin, N. A., Missler, D., Mounsor, D., Neftel, A., Nelson, C., Nemitz, E.,

569   Oudwater, R., Pascale, C., Petit, J.-E., Pogany, A., Redon, N., Sintermann, J.,

570   Stephens, A., Sutton, M. A., Tang, Y. S., Zijlmans, R., Braban, C. F., and

571   Niederhauser, B.: Intercomparison of in situ measurements of ambient NH_3:

572   instrument performance and application under field conditions, Atmos. Meas.

573   Tech. 15, 6755–6787, https://doi.org/10.5194/amt-15-6755-2022, 2022.

574 Wang, C., Yin, S., Bai, L., Zhang, X., Gu, X., Zhang, H., Lu, Q., and Zhang, R.: High-

575   resolution ammonia emission inventories with comprehensive analysis and

576   evaluation in Henan, China, 2006–2016, Atmos. Environ. 193, 11–23,

577   https://doi.org/10.1016/j.atmosenv.2018.08.063, 2018.

578 Wang, S., Wang, L., Li, Y., Wang, C., Wang, W., Yin, S., and Zhang, R.: Effect of

579   ammonia on fine-particle pH in agricultural regions of China: comparison between

580   urban and rural sites, Atmos. Chem. Phys., 20, 2719–2734,

581   https://doi.org/10.5194/acp-20-2719-2020, 2020.

582 Wang, S., Wang, L., Fan, X., Wang, N., Ma, S., and Zhang, R.: Formation pathway of

583   secondary inorganic aerosol and its influencing factors in Northern China:

584   Comparison between urban and rural sites, Sci. Total Environ., 840,

585   https://doi.org/10.1016/j.scitotenv.2022.156404, 2022.

586 Wang, S., Fan, X., Xu, Y., Zhang, R., and Ren, B.: Insight into the non-linear responses

587   of particulate sulfate to reduced SO_2 concentration: A perspective from the

aqueous-phase reactions in a megacity in Northern China, Atmos. Res., 290, https://doi.org/10.1016/j.atmosres.2023.106796, 2023a.

Wang, W., Wang, S., Xu, J., Zhou, R., Shi, C., and Zhou, B.: Gas-phase ammonia and $PM_{2.5}$ ammonium in a busy traffic area of Nanjing, China, Environ. Sci. Pollut. Res. Int., 23, 1691–1702, https://doi.org/10.1007/s11356-015-5397-3, 2016.

Wang, Y., Jin, X., Liu, Z., Wang, G., Tang, G., Lu, K., Hu, B., Wang, S., Li, G., An, X., Wang, C., Hu, Q., He, L., Zhang, F., and Zhang, Y.: Progress in quantitative research on the relationship between atmospheric oxidation and air quality, J. Environ. Sci., 123, 350–366, https://doi.org/10.1016/j.jes.2022.06.029, 2023b.

Wells, M., Choularton, T. W., and Bower, K. N.: A modelling study of the interaction of ammonia with cloud., Atmos. Environ., 32, 359–363, https://doi.org/10.1016/s1352-2310(97)00199-4, 1998.

Wentworth, G. R., Murphy, J. G., Benedict, K. B., Bangs, E. J., and Collett Jr, J. L.: The role of dew as a night-time reservoir and morning source for atmospheric ammonia, Atmos. Chem. Phys. 16, 7435–7449, https://doi.org/10.5194/acp-16-7435-2016, 2016.

Wu, C., Lv, S., Wang, F., Liu, X., Li, J., Liu, L., Zhang, S., Du, W., Liu, S., Zhang, F., Li, J., Meng, J., and Wang, G.: Ammonia in urban atmosphere can be substantially reduced by vehicle emission control: A case study in Shanghai, China, J. Environ. Sci., 126, 754–760, https://doi.org/10.1016/j.jes.2022.04.043, 2023.

Xie, Y., Wang, G., Wang, X., Chen, J., Chen, Y., Tang, G., Wang, L., Ge, S., Xue, G., Wang, Y., and Gao, J.: Nitrate-dominated PM2.5 and elevation of particle pH

observed in urban Beijing during the winter of 2017. Atmos. Chem. Phys. 20, 5019–5033, https://doi.org/10.5194/acp-20-5019-2020, 2020.

Xing, L., Fu, T. M., Cao, J. J., Lee, S. C., Wang, G. H., Ho, K. F., Cheng, M. C., You, C. F., and Wang, T. J.: Seasonal and spatial variability of the OM/OC mass ratios and high regional correlation between oxalic acid and zinc in Chinese urban organic aerosols, Atmos. Chem. Phys., 13, 4307–4318, https://doi.org/10.5194/acp-13-4307-2013, 2013.

Xu, J., Chen, J., Zhao, N., Wang, G., Yu, G., Li, H., Huo, J., Lin, Y., Fu, Q., Guo, H., Deng, C., Lee, S.-H., Chen, J., and Huang, K.: Importance of gas-particle partitioning of ammonia in haze formation in the rural agricultural environment, Atmos. Chem. Phys. 20, 7259–7269, https://doi.org/10.5194/acp-20-7259-2020, 2020.

Xu, W., Kuang, Y., Zhao, C., Tao, J., Zhao, G., Bian, Y., Yang, W., Yu, Y., Shen, C., Liang, L., Zhang, G., Lin, W., and Xu, X.: NH_3-promoted hydrolysis of NO_2 induces explosive growth in HONO, Atmos. Chem. Phys. 19, 10557–10570, https://doi.org/10.5194/acp-19-10557-2019, 2019.

Xu, W., Zhao, Y., Wen, Z., Chang, Y., Pan, Y., Sun, Y., Ma, X., Sha, Z., Li, Z., Kang, J., Liu, L., Tang, A., Wang, K., Zhang, Y., Guo, Y., Zhang, L., Sheng, L., Zhang, X., Gu, B., Song, Y., Van Damme, M., Clarisse, L., Coheur, P. F., Collett, J. L., Jr., Goulding, K., Zhang, F., He, K., and Liu, X.: Increasing importance of ammonia emission abatement in $PM_{2.5}$ pollution control. Sci. Bull. 67, 1745–1749, https://doi.org/10.1016/j.scib.2022.07.021, 2022.

632   Xue, C.: Substantially growing interest in the chemistry of nitrous acid (HONO) in

633   China: current achievements, problems, and future directions. Environ. Sci.

634   Technol. 56, 7375–7377. https://doi.org/10.1021/acs.est.2c02237, 2022.

635   Ye, C., Zhang, N., Gao, H., and Zhou, X.: Photolysis of particulate nitrate as a source

636   of HONO and NO_x. Environ. Sci. Technol. 51, 6849–6856,

637   https://doi.org/10.1021/acs.est.7b00387, 2017.

638   Ye, X., Ma, Z., Zhang, J., Du, H., Chen, J., Chen, H., Yang, X., Gao, W., and Geng, F.:

639   Important role of ammonia on haze formation in Shanghai, Environ. Res. Lett. 6,

640   024019, https://doi.org/10.1088/1748-9326/6/2/024019, 2011.

641   Zhang, W., Tong, S., Jia, C., Wang, L., Liu, B., Tang, G., Ji, D., Hu, B., Liu, Z., Li, W.,

642   Wang, Z., Liu, Y., Wang, Y., and Ge, M.: Different HONO sources for three layers

643   at the urban area of Beijing. Environ. Sci. Technol. 54, 12870–12880,

644   https://doi.org/10.1021/acs.est.0c02146, 2020a.

645   Zhang, W., Tong, S., Jia, C., Ge, M., Ji, D., Zhang, C., Liu, P., Zhao, X., Mu, Y., Hu, B.,

646   Wang, L., Tang, G., Li, X., Li, W., and Wang, Z.: Effect of different combustion

647   processes on atmospheric nitrous acid formation mechanisms: a winter

648   comparative observation in urban, suburban and rural areas of the North China

649   Plain. Environ. Sci. Technol. 56, 4828–4837,

650   https://doi.org/10.1021/acs.est.1c07784, 2022.

651   Zhang, Y., Liu, X., Fang, Y., Liu, D., Tang, A., and Collett, J. L.: Atmospheric ammonia

652   in Beijing during the COVID-19 outbreak: concentrations, sources, and

653   implications. Environ. Sci. Technol. Lett. 8, 32–38,

654   https://doi.org/10.1021/acs.estlett.0c00756, 2020b.

 Figures:

656
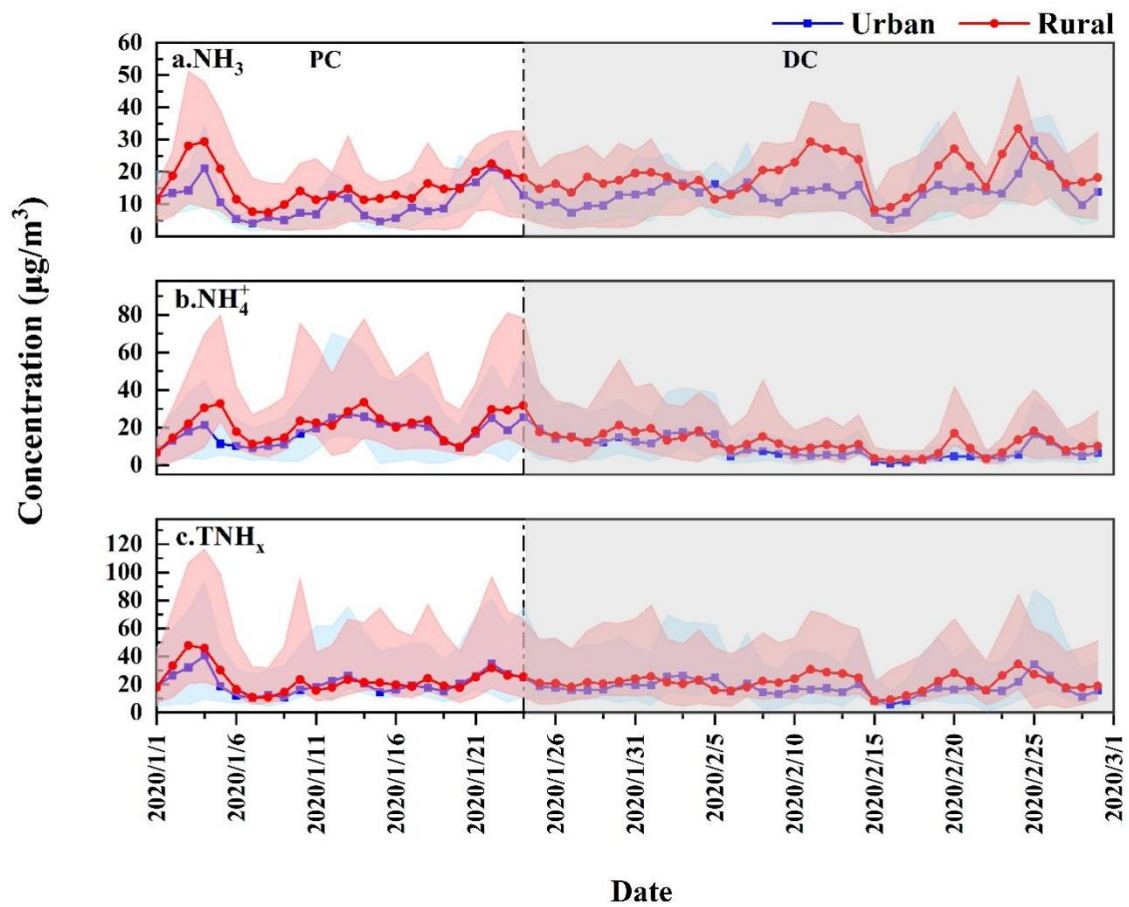
Figure 1.   Temporal variations of a. NH_3, b. NH_4^+, and c. TNH_x at the urban and rural

sites before (PC) and during (DC) the COVID-19 outbreak, respectively. The shaded

areas of the curve represent the maximum and minimum values.
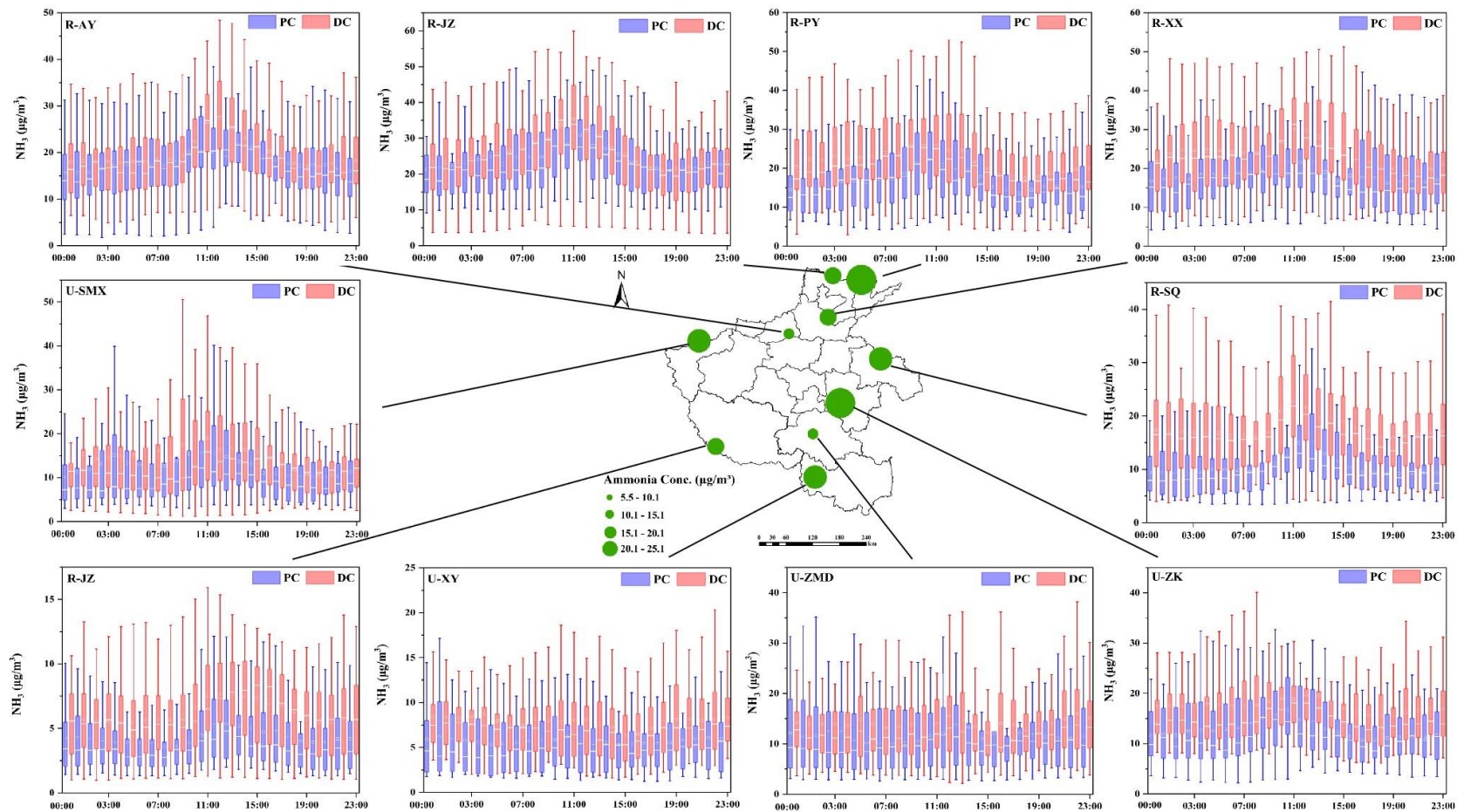
660
661 Figure 2. Daily variation of NH$_3$ concentrations at ten sites before (PC) and during (DC) the COVID-19 outbreak. The green dots represent the
662 location of ten sites and their size represents the concentration of NH$_3$; In each box, the top, middle, and bottom lines represent the 75, 50, and 25
663 percentiles of statistical data, respectively; the upper and lower whiskers represent the 90 and 10 percentiles of statistical data, respectively.

664
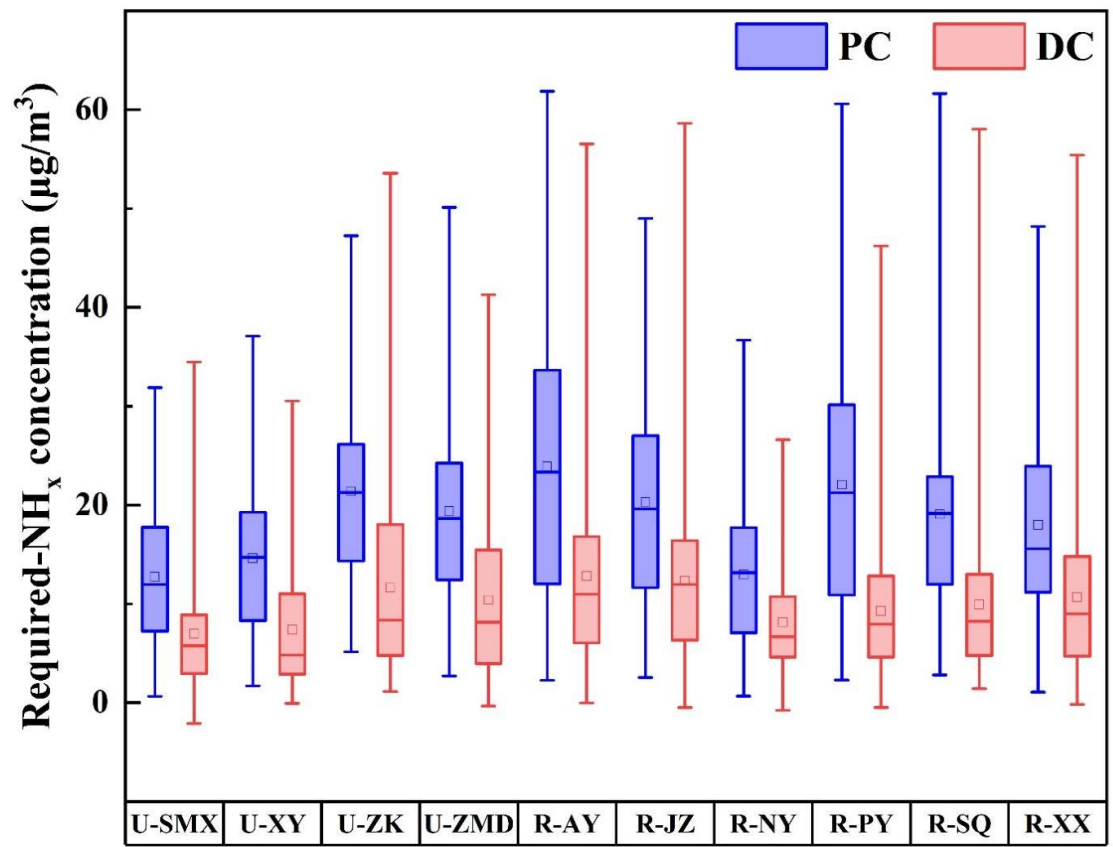
Figure 3. Box diagram of changes in Required-NH$_x$ at ten sites before (PC) and during

(DC) the COVID-19 outbreak. In each box, the top, middle, and bottom lines represent

the 75, 50, and 25 percentiles of statistical data, respectively; the upper and lower

whiskers represent the 90 and 10 percentiles of statistical data, respectively.

669
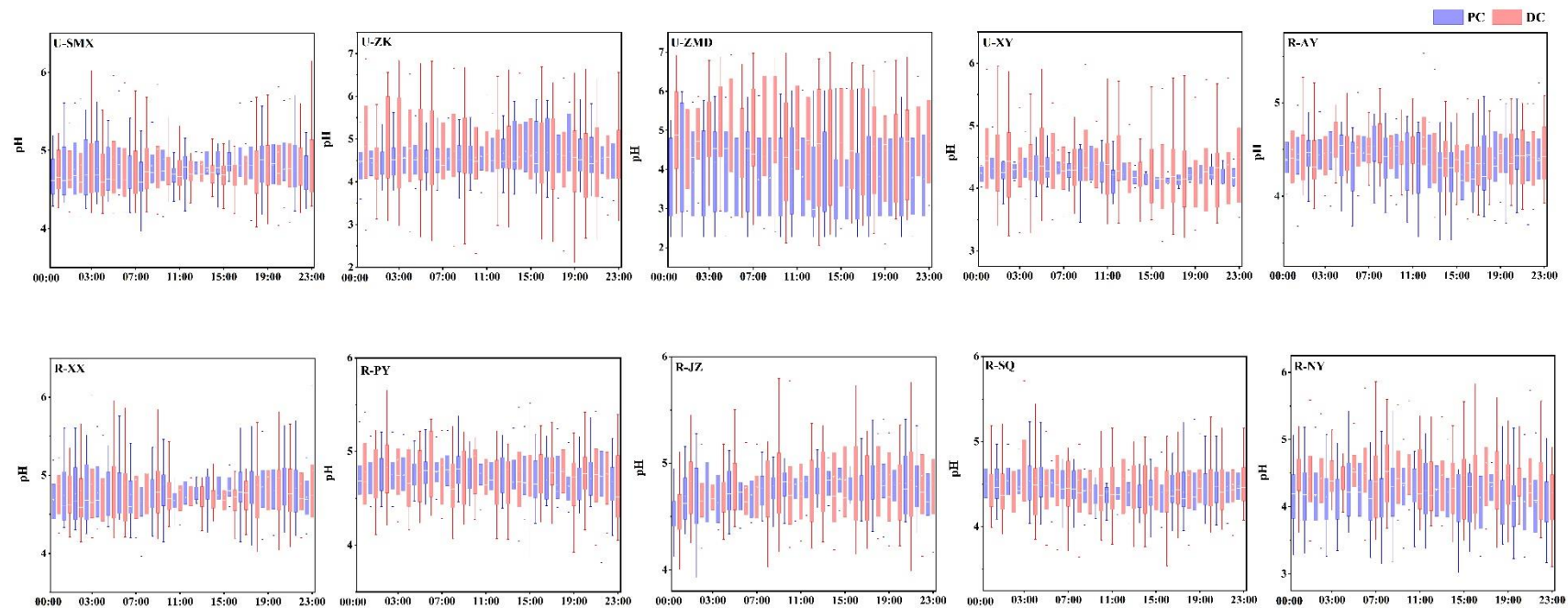
Figure 4.   Diurnal patterns of pH at ten sites before (PC) and during (DC) the COVID-19 outbreak. In each box, the top, middle, and bottom

lines represent the 75, 50, and 25 percentiles of statistical data, respectively; the upper and lower whiskers represent the 90 and 10 percentiles of

statistical data, respectively.
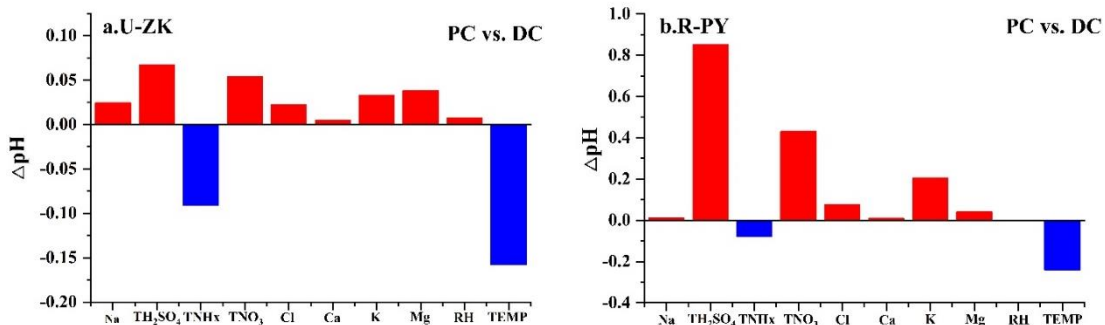
673

674   Figure 5. Changes of pH (ΔpH) through the sensitivity tests (Figure S5 and S6) by

675   changing parameters between PC and DC at the a. U-ZK and b. R-PY sites.
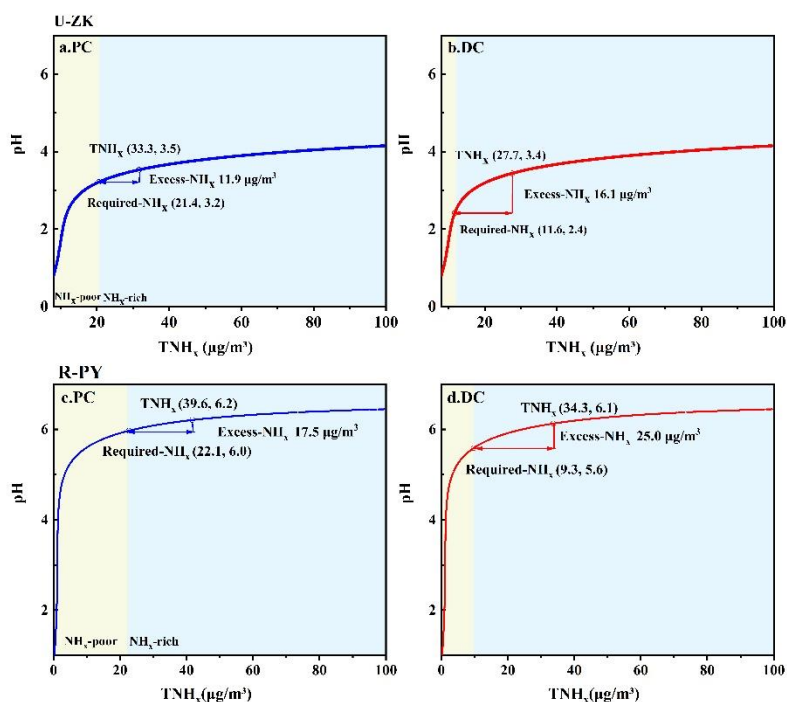
676

677   Figure 6. Particle pH corresponds to increasing TNH_x at U-ZK and R-PY sites to

678   examine the effects of major indicators of NH_3 (i.e., TNH_x, Required-NH_x, and Excess-

679   NH_x) on aerosol acidity. Particle pH was calculated by using a wide range of TNH_x

680   (25–130 $\mu g/m^3$) and average values of other parameters in PC and DC of U-ZK and R-

681   PY sites. The concentrations of TNH_x, Required-NH_x, and Excess-NH_x with

682   corresponding pH values are marked by a hollow box, hollow circle, and arrow

683   respectively. The yellow and blue background colors correspond to the NH_x-poor and

684   NH_x-rich, respectively.
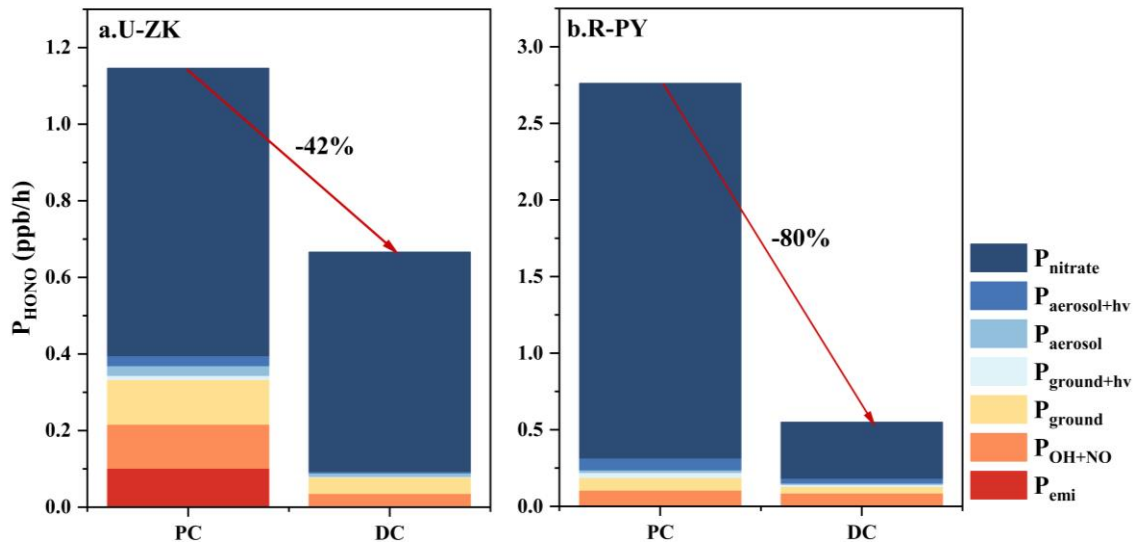
685

686 Figure 7. Comparison of HONO sources at a. U-ZK and b. R-PY sites before (PC) and

687 during (DC) the COVID-19 outbreak. The calculation method can be found in Text S4.

688
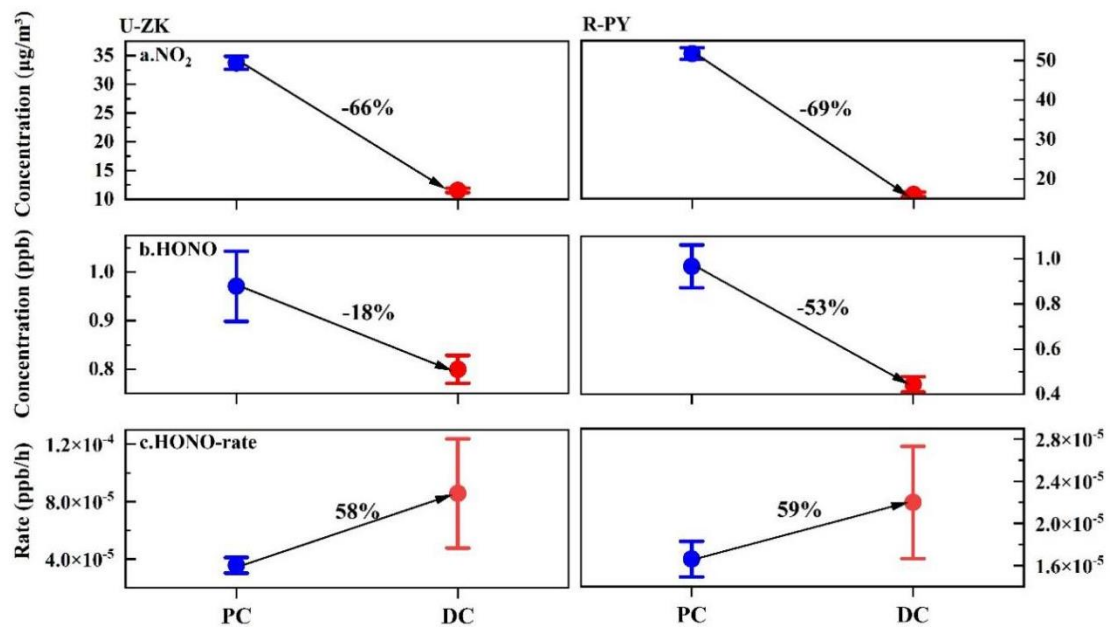
689

690 Figure 8. Decline ratios of a. NO$_2$, b. HONO concentration, and c. HONO production

691 rate at U-ZK and R-PY sites before (PC) and during (DC) the COVID-19 outbreak. The

692 center point represents the mean value, and the upper and lower whiskers represent the

693 95% confidence interval of the mean.

694 **Table:**

695 Table 1. Changes in concentrations (mean ± standard deviation) of NH_3, NH_4^+, and

696 TNH_x at ten sites during entire periods (Average), before (PC), and during (DC) the

697 COVID-19 outbreak.

Sites	Substances	Average (µg/m³)	PC (µg/m³)	DC (µg/m³)
U-SMX	NH_3	13.8 ± 10.8	12.6 ± 10.1	14.5 ± 11.1
	NH_4^+	10.9 ± 7.2	14.2 ± 7.2	8.8 ± 6.5
	TNH_x	22.9 ± 14.1	24.9 ± 14.5	21.7 ± 13.8
U-ZK	NH_3	15.6 ± 8.3	12.7 ± 6.5	17.4 ± 8.8
	NH_4^+	13.6 ± 9.3	19.1 ± 8.4	10.3 ± 8.1
	TNH_x	28.6 ± 13.7	30.9 ± 12.8	27.1 ± 14.0
U-ZMD	NH_3	13.1 ± 8.4	11.6 ± 8.2	14.0 ± 8.4
	NH_4^+	13.9 ± 9.8	19.6 ± 10.3	10.3 ± 7.5
	TNH_x	25.7 ± 14.6	30.3 ± 15.1	22.8 ± 13.5
U-XY	NH_3	7.0 ± 4.3	5.7 ± 4.0	7.9 ± 4.3
	NH_4^+	11.0 ± 7.7	15.4 ± 7.6	8.3 ± 6.5
	TNH_x	17.6 ± 9.8	20.6 ± 10.1	15.7 ± 9.2
R-AY	NH_3	19.0 ± 8.4	17.9 ± 8.3	19.7 ± 8.4
	NH_4^+	19.3 ± 12.9	26.4 ± 13.7	15.0 ± 10.3
	TNH_x	36.6 ± 18.2	41.7 ± 20.4	33.4 ± 16.0
R-XX	NH_3	21.7 ± 10.2	18.1 ± 9.3	23.8 ± 10.1
	NH_4^+	15.9 ± 10.4	20.6 ± 11.0	13.0 ± 8.8
	TNH_x	34.9 ± 17.0	35.1 ± 18.8	34.8 ± 15.8
R-PY	NH_3	19.8 ± 9.4	16.8 ± 8.1	21.7 ± 9.6
	NH_4^+	17.4 ± 11.8	25.3 ± 12.6	12.4 ± 8.0
	TNH_x	35.2 ± 17.8	39.4 ± 19.8	32.6 ± 15.7
R-JZ	NH_3	25.3 ± 11.5	24.1 ± 11.5	25.9 ± 11.4
	NH_4^+	17.3 ± 11.3	22.7 ± 11.6	14.2 ± 9.9
	TNH_x	40.8 ± 20.1	42.9 ± 22.8	33.5 ± 18.2
R-SQ	NH_3	15.0 ± 7.9	10.3 ± 5.2	17.7 ± 7.9
	NH_4^+	13.4 ± 8.5	18.9 ± 8.6	10.3 ± 6.7
	TNH_x	26.3 ± 13.2	25.5 ± 14.0	26.8 ± 12.7
R-NY	NH_3	5.5 ± 3.1	4.3 ± 2.7	6.2 ± 3.2
	NH_4^+	10.2 ± 6.9	13.3 ± 7.2	8.4 ± 6.1
	TNH_x	14.8 ± 8.5	16.0 ± 9.5	14.1 ± 7.8

698